AGU PUBLICATIONS

JGR

Journal of Geophysical Research: Atmospheres

RESEARCH ARTICLE
10.1002/2016JD025408

Deep convective cloud characterizations from both broadband imager and hyperspectral infrared sounder measurements

Yufei Ai[1,2], Jun Li[2], Wenjing Shi[2,3], Timothy J. Schmit[4], Changyong Cao[4], and Wanbiao Li[1]

[1]Laboratory for Climate and Ocean-Atmosphere Studies, Department of Atmospheric and Oceanic Sciences, School of Physics, Peking University, Beijing, China, [2]Cooperative Institute for Meteorological Satellite Studies, University of Wisconsin-Madison, Madison, Wisconsin, USA, [3]State Key Laboratory of Numerical Modeling for Atmospheric Sciences and Geophysical Fluid Dynamics, Institute of Atmospheric Physics, Chinese Academy of Sciences, Beijing, China, [4]Center for Satellite Applications and Research, NESDIS/NOAA, Silver Spring, Maryland, USA

Key Points:
- Discussion of DCC detection with BNR from different instruments
- Uncertainty in the DCC identification using broadband and hyperspectral infrared instruments
- Relationship between the DCC top height and infrared BTD

Correspondence to:
J. Li,
jun.li@ssec.wisc.edu

Citation:
Ai, Y., J. Li, W. Shi, T. J. Schmit, C. Cao, and W. Li (2017), Deep convective cloud characterizations from both broadband imager and hyperspectral infrared sounder measurements, *J. Geophys. Res. Atmos.*, *122*, 1700–1712, doi:10.1002/2016JD025408.

Received 24 MAY 2016
Accepted 11 JAN 2017
Accepted article online 14 JAN 2017
Published online 2 FEB 2017

Abstract Deep convective storms have contributed to airplane accidents, making them a threat to aviation safety. The most common method to identify deep convective clouds (DCCs) is using the brightness temperature difference (BTD) between the atmospheric infrared (IR) window band and the water vapor (WV) absorption band. The effectiveness of the BTD method for DCC detection is highly related to the spectral resolution and signal-to-noise ratio (SNR) of the WV band. In order to understand the sensitivity of BTD to spectral resolution and SNR for DCC detection, a BTD to noise ratio method using the difference between the WV and IR window radiances is developed to assess the uncertainty of DCC identification for different instruments. We examined the case of AirAsia Flight QZ8501. The brightness temperatures (T_bs) over DCCs from this case are simulated for BTD sensitivity studies by a fast forward radiative transfer model with an opaque cloud assumption for both broadband imager (e.g., Multifunction Transport Satellite imager, MTSAT-2 imager) and hyperspectral IR sounder (e.g., Atmospheric Infrared Sounder) instruments; we also examined the relationship between the simulated T_b and the cloud top height. Results show that despite the coarser spatial resolution, BTDs measured by a hyperspectral IR sounder are much more sensitive to high cloud tops than broadband BTDs. As demonstrated in this study, a hyperspectral IR sounder can identify DCCs with better accuracy.

1. Introduction

Deep convective cloud s (DCCs) are associated with severe storms, which can transport ice and supercooled large droplets into the higher levels of the atmosphere to create conditions conducive to icing [*Reynolds*, 1980; *Setvák et al.*, 2008, 2013; *Bedka et al.*, 2010]. In addition, severe convective storms also cause turbulence near the tropopause [*Lane et al.*, 2003]. An environment prone to icing and strong turbulence poses threats to aviation safety. On 28 December 2014, AirAsia Flight QZ8501 crashed into the Java Sea during a period of convective storms in the region. Similarly, Air France Flight AF447 crashed into the Atlantic Ocean on 1 June 2009 near a convection zone. Detecting DCCs has significant implications for preventing potential aviation accidents.

Satellite remote sensing offers several methods to identify the overshooting tops (OTs) of DCCs. One simple method is using a fixed brightness temperature (T_b) threshold for the IR window channel centered near 11 μm. The fixed T_b is widely used in the life cycle study of weather systems containing DCCs [*Machado et al.*, 1998; *Mathon and Laurent*, 2001; *Ai et al.*, 2016]. However, the optimal threshold varies with the latitude, longitude, and the composition of the cloud top and should be determined from research based on different studying regions and periods [*Mapes and Houze*, 1993; *Aumann et al.*, 2011]. The IR channel T_b is only sensitive to the cloud top, so that sometimes high cirrus and an anvil without any precipitation are still identified as deep convection by some fixed T_b thresholds. Considering this shortcoming of the fixed T_b threshold, a new technique called the infrared window-texture method is proposed by *Bedka et al.* [2010]. This method integrates the IR channel T_b gradients, numerical weather prediction (NWP) tropopause temperature forecast, and OT size and T_b criteria from Moderate Resolution Imaging Spectroradiometer (MODIS) and Advanced Very High Resolution Radiometer (AVHRR) imagery, increasing the detectability of OTs from geostationary imager data [*Bedka*, 2011; *Bedka et al.*, 2012]. However, this method cannot detect OTs for small and newly developing convective cloud with limited anvil cloud content. The detection also requires NWP data which might not synchronize

with satellite observations; in addition, a direct broadcast user who uses the satellite data and products might not be able to access the full resolution numerical weather prediction (NWP) data.

The brightness temperature difference (BTD) method is another common method for DCC identification. Cases where the brightness temperature in the water vapor (WV) absorption channel is warmer than that in the atmospheric infrared window (IR) channel (BTD $= T_{b,\mathrm{WV}} - T_{b,\mathrm{IR}} \geq 0$) were interpreted as convective OTs [*Ackerman*, 1996; *Schmetz et al.*, 1997]. The positive difference signifies convective overshooting because water vapor above the physical cloud top which is forced into the lower stratosphere by storm updraft emits at the warmer stratospheric temperature, while the IR window channel shows emission from the colder cloud top. With the BTD method, DCCs and convective OTs are monitored with imagers onboard geostationary satellites around the globe [*Schmetz et al.*, 1997; *Bedka et al.*, 2010; *Aumann and Ruzmaikin*, 2013]. In addition, BTD can be used to monitor other weather systems with high cloud tops such as typhoons, as well as estimate heavy precipitation within DCCs [*Kurino*, 1997; *Machado et al.*, 2009]. Based on simple BTD method, the method for objective detection of DCCs described in this paper can be used in climate studies such as East China Monsoon [*Tang and Chen*, 2006; *Wu et al.*, 2013; *Qie et al.*, 2014] and serve as input to NWP models or as part of other sophisticated algorithms [*Chemel et al.*, 2009; *Setvák et al.*, 2008].

Ackerman [1996] found that a BTD larger than 2 K should be attributed to optically thick clouds of overshooting convection, but calibration errors, bit depth, and nonuniform scenes within the field of view of a broadband imager could still result in a positive BTD. Although the calibration has been improved significantly, this method is still limited by the bit depth of the sensor. In addition, based on previous research for geostationary satellite imagers, positive BTD values are not only attributable to the warmer water vapor above the storm top but also due to scattering or emissivity effects in thin cirrus at or above the cloud top [*Setvák et al.*, 2013]. Prior studies have shown that the BTD threshold, however, is a function of the spatial resolution. For instance, for the current generation of the GOES imager with 4 km spatial resolution, a BTD value greater than 1 K is used to show OT [*Martin et al.*, 2008], while for high-resolution imagery such as MODIS (1 km), 2 K is a better indicator of OT [*Bedka et al.*, 2010]. All the research mentioned above is based on measurements from imagers. When the WV-IR BTD does not perform very well for overshooting clouds, it is often due to the nature of broadband, as the current satellite WV band especially has wide spectral coverage. *Aumann and Ruzmaikin* [2013] used BTD measured by the hyperspectral Atmospheric Infrared Sounder (AIRS) to identify DCCs in order to avoid the ambiguity caused by the wide bandwidth of broadband imagers and concluded that the hyperspectral sounder improved DCC identification. With hyperspectral instruments such as AIRS, the Infrared Atmospheric Sounding Interferometer (IASI) [*Chalon et al.*, 2001] and Cross-track Infrared Sounder (CrIS) [*Bloom*, 2001], the BTD can be derived from weak and strong water vapor absorption channels, which makes the BTD signal much stronger than that from broadband instruments. However, the sensitivity of the BTD method to the spectral resolution and signal-to-noise ratio (SNR) for DCC identification remains unclear. While the relationship between the height of the convective overshooting clouds and BTD has been statistically described by previous research [e.g., *Young et al.*, 2012], it has not been fully investigated. Additionally, the performance of the BTD method by the new generation instruments, such as the Advanced Himawari Imager (AHI) [*Kurino*, 2012], the Advanced Baseline Imager (ABI) [*Schmit et al.*, 2005, 2009, 2017], and the Visible Infrared Imager Radiometer Suite (VIIRS) [*Welsch et al.*, 2001], has not been assessed to show the effects of better spectral resolution and smaller instrument noise.

In order to understand the sensitivity of BTD to the spectral resolution and SNR for DCC detection, a new index called the BTD to noise ratio (BNR) is defined to assess the performance of different instruments to detect DCCs. By applying this index, the uncertainty in DCC identification by both broadband and hyperspectral infrared instruments is determined; the sensitivity of BTD to cloud top height (CTH) is studied with a fast radiative transfer model (RTM). In this paper, the term band refers specifically to a broadband IR imager, and channel refers specifically to a hyperspectral IR sounder. Spectral resolution is described by the total number of spectral bands/channels on an instrument. The brightness temperatures of IR window and WV bands/channels are simulated for both broadband and hyperspectral IR instruments using an RTM to study the relationship between T_b and CTH. In addition, satellite images related to the QZ8501 and AF447 cases, as well as Typhoon Haiyan and Typhoon Linfa, are analyzed using the BTD method to identify DCCs from both types of instruments.

Table 1. Information About the Instruments Used in This Study

Type of Instrument	Name	Platform	Providing Agency	Spatial Resolution	Data/Product	
Imager	IMAGER	MTSAT-2	JMA	4 km	T_b and NEΔT	10.8, 6.75 μm
	SEVIRI	MSG	EUMETSAT	3 km		10.8, 6.25 μm
	MI	COMS-1	KMA	4 km		10.8, 6.75 μm
	VIIRS	SNPP	NOAA	750 m		10.736, 6.70 μm[a]
	AHI	Himawari-8	JMA	2 km		10.45, 6.25 μm
Hyperspectral IR sounder	AIRS	Aqua	NASA	~13.5 km (nadir)	T_b and NEΔT	1231, 1419 cm^{-1}
	IASI	Metop-A/B	EUMETSAT	~12 km (nadir)		
Spectroradiometer	MODIS	Aqua	NASA	250 m to 1 km	Reflectivity	620–670 nm
Radar/Lidar	CPR/CALIOP	CloudSat/CALIPSO	NASA	1.4 km × 1.7 km × 500 m	2B-GEOPROF/2BGEOPROF-LIDAR	

[a]Simulated band.

2. Radiative Transfer Model and Observations

The Radiative Transfer for the TIROS (the Television Infrared Observation Satellite) Operational Vertical sounder (RTTOV) model was first developed in the early 1990s [*Eyre*, 1991; *Saunders et al.*, 1999; *Matricardi et al.*, 2001]. RTTOV is capable of radiative transfer calculations for various IR and microwave (MW) instruments. The model requires inputs such as atmospheric vertical profiles of temperature, water vapor concentration, cloud option, surface properties, and specific band information for radiances. The atmospheric profile inputs in this study are configured using standard atmospheric profiles of the tropics and the European Center for Medium-Range Weather Forecasting (ECMWF) operational analysis data set. A simple cloud scheme [*Eyre and Menzel*, 1989; *Li et al.*, 2001] is used in this study to simulate the DCCs, which assumes a black opaque cloud at a single cloud top level. The coefficient files for the simulated instruments are available in the latest RTTOV v11.2. It should be noted that for general cloud situations, both the molecular absorption and the cloud particle absorption/scattering are considered [*Wei et al.*, 2004] for brightness temperature calculations and cloud microphysical property retrievals [*Li et al.*, 2005a].

All the satellite instruments and products used in this study are listed in Table 1 with information on instrument type, name, satellite platform, providing agency, spatial resolution, and data or product used. Throughout this study the AIRS [*Aumann and Pagano*, 1994; *Aumann et al.*, 2003, 2006; *Aumann and Ruzmaikin*, 2013] on board the Earth Observing System (EOS) Aqua satellite is used as representative observations from a hyperspectral cross-nadir scanning IR sounder. In contrast, observations from moderate-resolution geostationary-based optical imagers vary from case to case based on the locations: for the QZ8501 case, the imager on board the Multifunction Transport Satellite 2 (MTSAT-2) [*Shimamura*, 1999] is used; the Spinning Enhanced Visible Infrared Imager (SEVIRI) on board Meteosat-9, the second flight unit of the Meteosat Second Generation (MSG) [*Aminou*, 2002; *Schmetz et al.*, 2002, 2003], is used in the analysis of the AF447 case; for the Typhoon Haiyan case, imagery from the Meteorological Imager (MI) on board the Communication, Ocean and Meteorological Satellite 1 (COMS-1) [*Cho and Youn*, 2006] is used; and for Typhoon Linfa, both the MTSAT-2 imager and AHI on board Himawari-8 [*Puschell et al.*, 2006] are included to compare instruments of two generations. The 1 km visible imagery (620–670 nm) from the Aqua MODIS is shown during the daytime to examine the cloud details observed in these cases. The products from CloudSat/CALIPSO (Cloud-Aerosol Lidar and Infrared Pathfinder Satellite Observations) [*Stephens et al.*, 2002] are matched with other observations if available to validate the cloud structure. The 2B-GEOPROF product from CloudSat provides an estimate of the radar reflectivity factor (unit dB*Z*) for vertical sample columns [*Marchand et al.*, 2008]. The 2B-GEOPROF-LIDAR product indicates the cloud fraction and the height of the detected cloud (unit km) measured by lidar [*Mace and Zhang*, 2014]. The sensitivity test of the angle effect is conducted by comparing the results between AIRS and AHI. Similarly, the sensitivity test of noise and spectral resolution comprises both broadband and hyperspectral IR instruments, including IASI [*Chalon et al.*, 2001], AIRS, MTSAT-2 imager, VIIRS, and AHI. Note that the VIIRS result is shown with the assumption that a WV band is added to VIIRS. There is one band centered at 6.70 μm simulated with the spectral response function of its 12.0 μm band in this section. This simulation gives VIIRS the same bands as MTSAT-2 but with much smaller noise, which shows the sensitivity of IR imagers

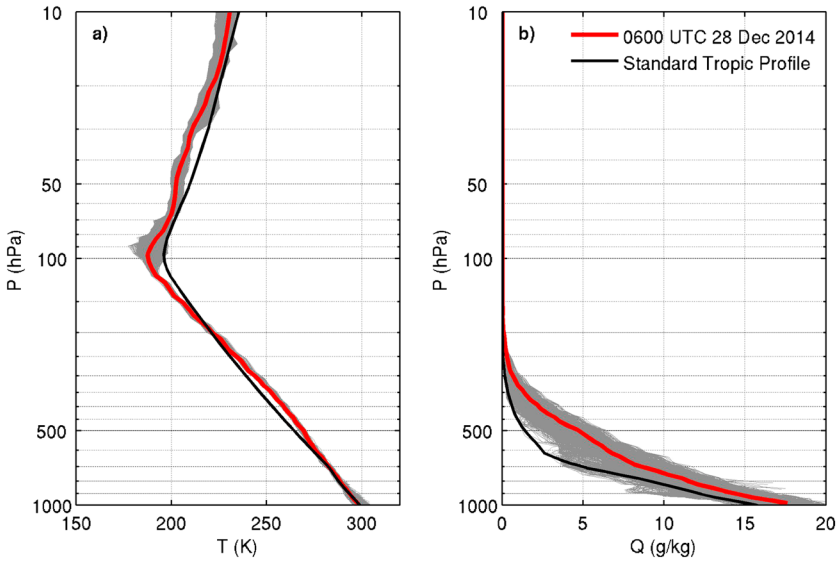

Figure 1. Input (a) *T* and (b) *Q* profiles. Grey lines are ECMWF analysis profiles in the domain. Red lines are the calculated mean value for *T* and *Q*. Black lines are the standard tropic profile.

to noise by BTD method. Since the reported noise is similar for MTSAT-2 and AHI, the comparison between these two instruments shows the sensitivity caused by improved spectral resolution. For the two hyperspectral instruments, IASI has better spectral resolution but larger noise than AIRS [*Chalon et al.*, 2001; *Aumann et al.*, 2003, 2006], so that the comparison indicates the sensitivity to both spectral resolution and noise. For the QZ8501 case, AHI is also included in the simulation study to compare the result with MTSAT-2 and AIRS.

3. Sensitivity of BTD Method

3.1. Angle Effect Evaluation

The T_bs of the pixels closer to the limb side of a satellite image often become colder than they actually are. This unique characteristic is called limb darkening due to the sensor scan angle [*Conway*, 1997]. In this angle effect experiment, the standard atmospheric profiles of the tropics and the vertical profiles for the QZ8501 case are used as the RTTOV input. For the QZ8501 case, the profiles were calculated as the mean value of the ECMWF operational analysis data set at 0600 UTC 28 December 2014 (temperature and moisture profiles shown in Figures 1a and 1b, respectively). The figure shows that the environment of this deep convection case has a larger temperature lapse rate compared to the standard atmospheric tropical profiles—warmer in the middle troposphere from 200 to 500 hPa and colder in the upper atmosphere (over 200 hPa). water vapor is also more abundant through the whole troposphere. Since the cloud tops of DCCs are near the tropopause, we set the cloud top pressure as 100, 200, and 300 hPa for the simulation while the satellite zenith angle varies from 0 to 60°. The differences between the T_b of a certain satellite zenith angle and the T_b of nadir ($\Delta T_b(\theta) = T_b(\theta) - T_b(0)$) are shown in Figure 2 for different bands/channels and different cloud top pressures.

In Figure 2, for simple clouds whose CTH is at 200 and 300 hPa, the T_b becomes colder (shown as negative ΔT_b in Figure 2) with an increase in satellite zenith angle, and the colder T_b with a larger zenith angle is because the radiation has traveled a longer distance through the atmosphere, resulting in more radiation being absorbed or scattered. In contrast, when the cloud top reaches 100 hPa in the stratosphere, the edge becomes warmer (shown as positive ΔT_b in Figure 2) than nadir since the emission comes from the warmer stratospheric temperature. The WV band/channel is more sensitive to the satellite zenith angle than the IR band/channel. When comparing the results of the two kinds of profiles (left and right columns of Figure 2), the limb side effect is more significant in the deep convective environment, especially for WV band/channel. The angle effect is negligible for the IR bands/channels, but the limb side effect from the WV band/channel produces errors for the BTD method especially in the deep convective environment. It can be indicated in the figure that the distortion in T_b is within ± 1 K with $\theta \leq 50°$, since the overshooting top height is usually between 100 and 200 hPa. Therefore, the angle effect is not significant for the BTD method when identifying DCCs even on the edge of the AIRS granule.

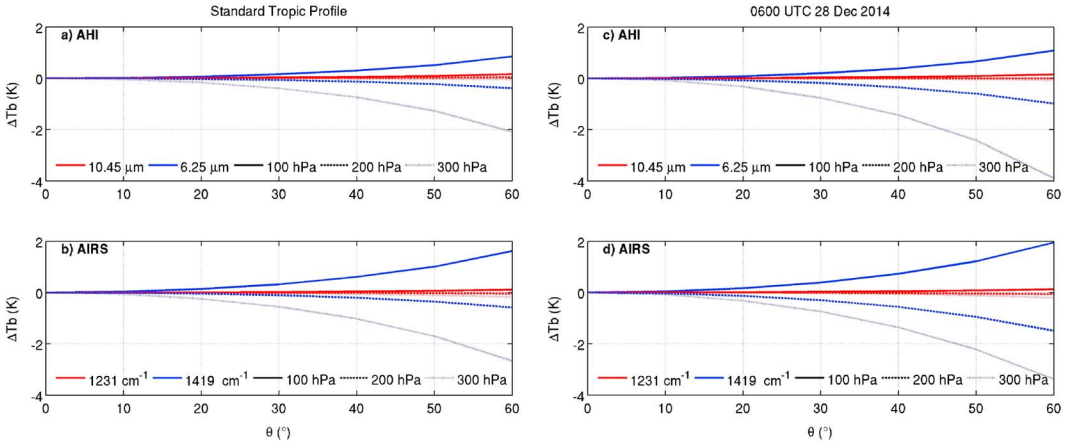

Figure 2. Angle effects illustrated by simulating standard tropic profiles (shown in Figure 1) and profiles at 0600 UTC 28 December 2014. The two instruments shown are (a, c) AHI and (b, d) AIRS. θ is the angle of satellite zenith and $\Delta T_b(\theta) = T_b(\theta) - T_b(0)$ showing the difference in T_b due to satellite zenith. The red lines are for atmospheric window channels, and the blue lines are for WV channels. The solid lines, the dashed lines, and the dotted lines are the results when cloud top pressures are 100, 200, and 300 hPa, respectively.

3.2. Impact of NEΔT and Spectral Resolution

The IR sensor detector noise is usually described as the noise-equivalent differential temperature (NEΔT). It is defined as the amount of infrared radiation to produce an output signal equal to the system's own noise, which represents approximately the minimum temperature difference between two signals which the sensor can resolve. In this study, the NEΔT is calculated based on the reported sensor noise for each band/channel. The value of NEΔT is a function of the temperature at which the measurement is made (in Figure 3), and a colder measurement temperature tends to have a larger NEΔT. The noise of the BTD method involving two bands/channels is described as

$$\text{Noise} = \sqrt{\text{NE}\Delta T_{\text{IR}}^2 + \text{NE}\Delta T_{\text{WV}}^2} \tag{1}$$

where the two terms represent the NEΔT from the IR and WV channel/band, respectively. As shown in Figure 3, IR window bands have a smaller NEΔT than WV bands. Thus, for broadband instruments, the effectiveness of the BTD method for DCC detection is highly related to the NEΔT of the WV band. For hyperspectral IR sounders such as AIRS and IASI, however, the IR channels have as much noise as WV channels.

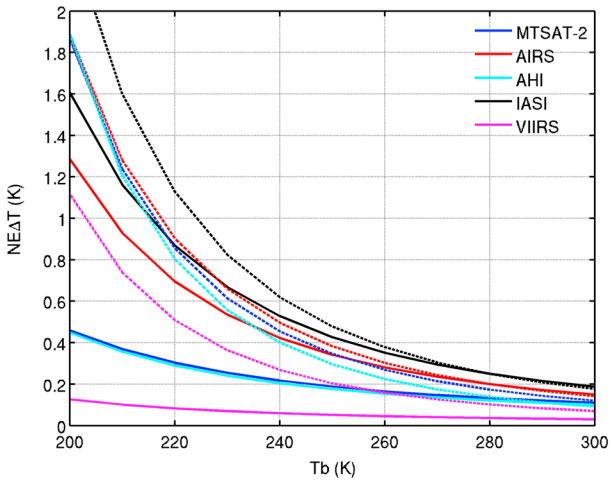

Figure 3. NEΔT of IR window bands/channels (solid lines) and WV bands/channels (dashed lines), respectively, for five instruments. The *x* axis shows the scene temperature.

A new index called the brightness temperature difference to noise ratio (BNR) for the BTD method is defined when BTD > 0 as

$$\text{BNR} = \frac{T_{b,\text{WV}} - T_{b,\text{IR}}}{\sqrt{\text{NE}\Delta T_{\text{IR}}^2 + \text{NE}\Delta T_{\text{WV}}^2}} \tag{2}$$

BNR = 1 means that the BTD is equal to the noise level. A BNR larger than 1 means that the BTD signal is stronger than the noise and the pixel is positively identified as the overshooting part of the DCC. Otherwise, a BNR less than 1 means that the positive BTD might be caused by noise and the pixel may be or may not be the overshooting part of the DCC. Larger values of BNR indicate a more accurate DCC detection for an instrument.

In Figure 4, the BNR of five instruments is simulated by RTTOV with the profiles from the QZ8501 case shown in Figure 1. Figures 4a

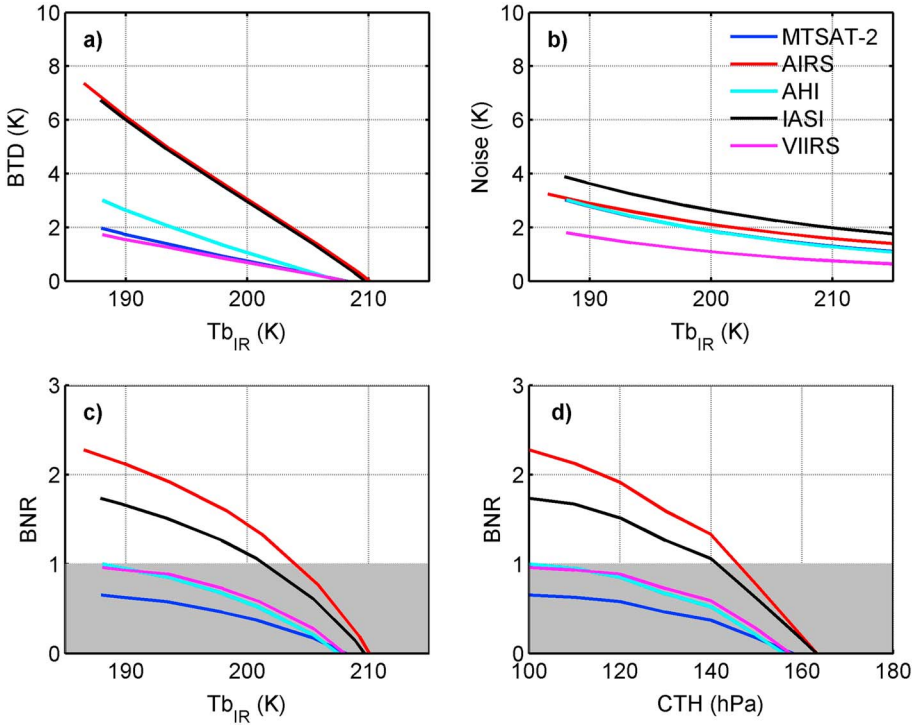

Figure 4. (a) Relationship between BTD and T_{bIR}. (b) Relationship between noise and T_{bIR}. (c) Relationships between BNR and T_{bIR}. (d) Relationships between BNR and CTH. The simulation for these five instruments uses profiles from the QZ8501 case (shown in Figure 1) by RTTOV.

and 4b display the relationships between the T_b of the IR bands/channels and the two terms in equation (2). As indicated in equation (2), either a larger BTD value or a smaller noise results in a larger BNR value. In these two panels both the BTD and noise grow larger as the cloud tops become higher, but the growth in BTD is more drastic than that in noise. Therefore, colder cloud tops result in a larger BNR as demonstrated in Figure 4c. Figure 4d shows BNR's relationships with CTH (unit hPa). BNR is larger than 1 when CTH is higher than 140 hPa, and the T_{bIR} is colder than 200 K for AIRS and IASI, and it continues to grow as the cloud ascends.

In this figure, BNR values from hyperspectral IR sounders such as AIRS and IASI are remarkably larger than those from imagers such as MTSAT-2, AHI, and VIIRS. AIRS has larger BNR values than IASI due to its smaller noise. For imagers, however, BNR is only close to 1 when clouds are much higher than the corresponding results from the sounders; in addition, it is not as sensitive to the CTH as the BNR from a hyperspectral IR sounder. In these panels, it is notable that the noise values of MTSAT-2, AHI, and AIRS are very similar. AIRS performs best due to the finer spectral resolution, and AHI seems better than MTSAT-2. VIIRS has BTD values similar to those from MTSAT-2 but with the least noise among the five instruments. As a result, it performs better than MTSAT-2, but its BNR is not as sensitive to CTH as AHI. It can be inferred that with additional WV channels on a future VIIRS, improved DCC detection will be possible. Thus, it seems that advances in spectral resolution lead to improvements in BNR for imagers, while smaller noise improves the performance for hyperspectral sounders.

4. Simulation Study for QZ8501 Case

The MTSAT-2 imager, AHI, and AIRS are used for simulation in the QZ8501 case. The real satellite zeniths as the middle pixel in the analysis domain (2°S, 110°E) are applied for all the instruments.

The relationships between CTH and T_b are illustrated in Figures 5a–5c. The critical cloud top pressure (CCTP) when BTD = 0 is used in this study as the minimum height where a convective cloud can be detected as a DCC if not considering noise. This parameter in DCC identification differs among instruments given certain atmospheric environments. The CCTP is very similar in the following situations: between 150 and 160 hPa for the MTSAT-2 imager and AHI and between 160 and 170 hPa for AIRS. The corresponding values of T_{bIR} at CCTP are about 208 K for the MTSAT-2 imager and AHI, while 210 K for AIRS. In Figure 5, the T_b for the IR band/channel is very similar since their wavelengths are both located in the atmospheric window zone with

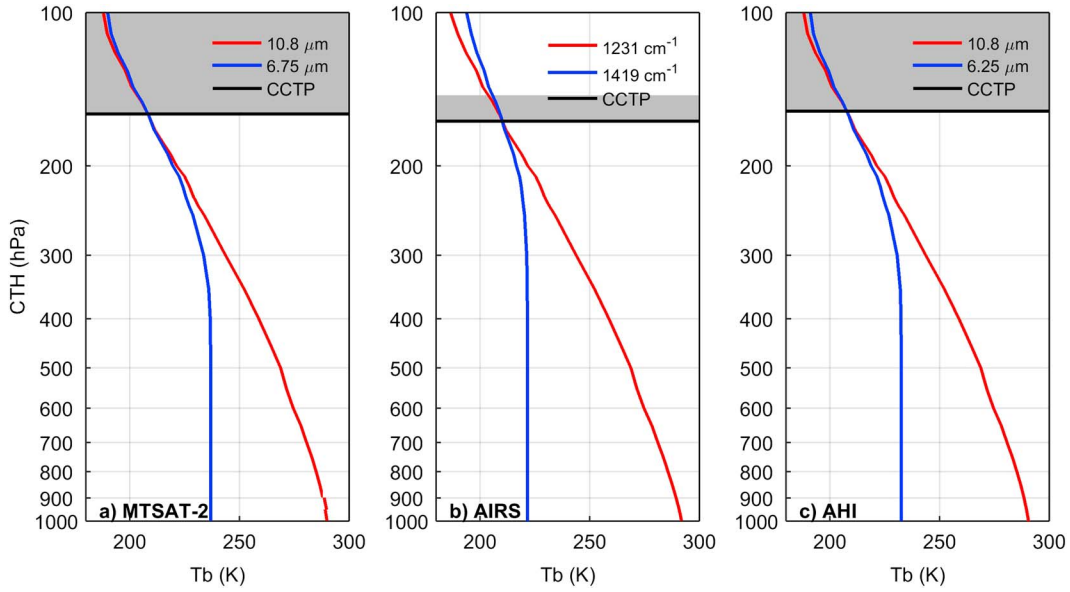

Figure 5. (a–c) The simulated relationships from RTTOV between cloud top pressure and simulated T_bs of the IR band/channel (red lines) and WV band/channel (blue lines) for MTSAT-2, AIRS, and AHI, respectively. The grey background denotes the ranges of CTH where BNR ≤ 1. The black line is the CCTP when BTD = 0.

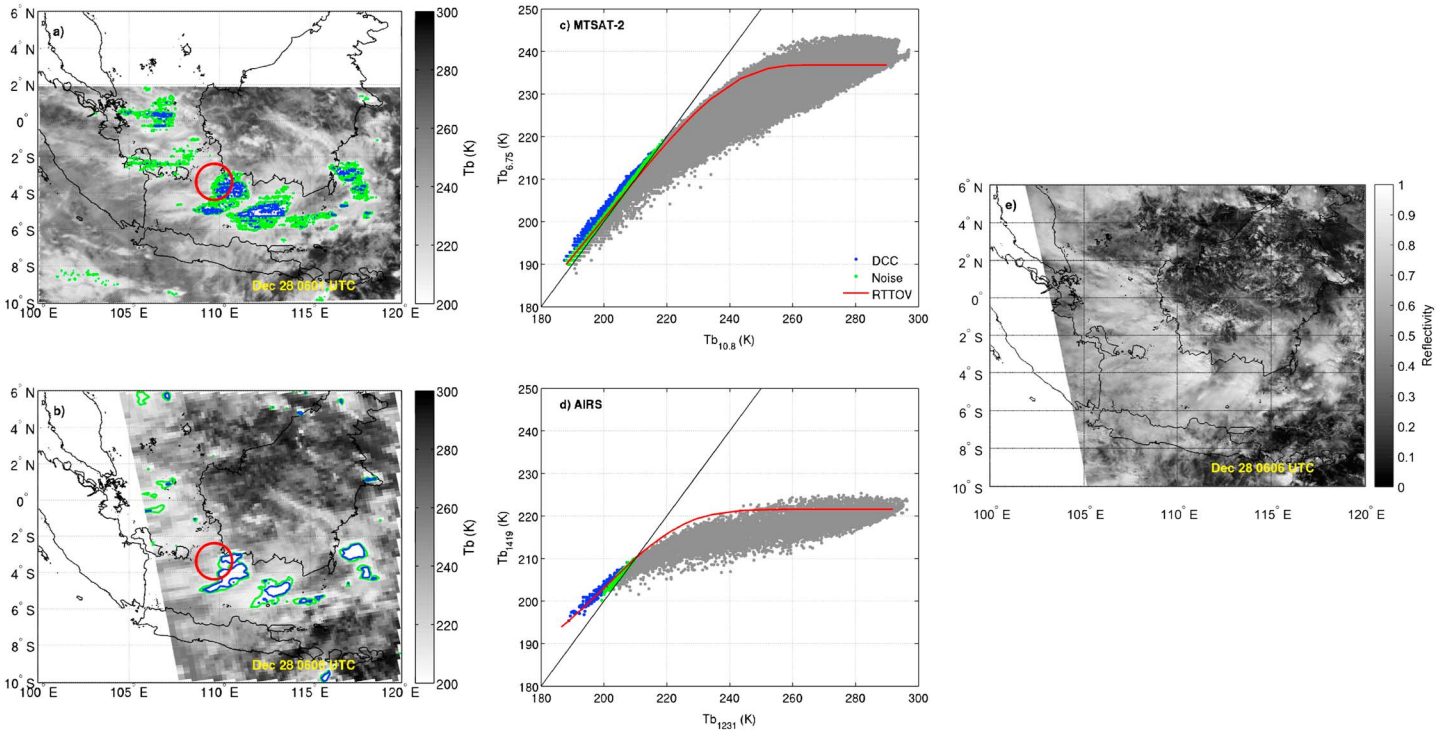

Figure 6. Brightness temperature images at 0600 UTC 28 December 2014 from the atmospheric IR window band/channel on (a) MTSAT-2 and (b) AIRS. The blue contours denote pixels where BNR = 1, and the green contours show pixels where BTD = 0. The red circles show the location where QZ8501 lost contact. The T_bs of both IR and WV channels for all pixels are displayed (c) from MTSAT-2 and (d) from AIRS: for MTSAT-2 (Figure 6c) the *x* axis and *y* axis are T_bs of 10.8 and 6.75 μm bands, respectively, and for AIRS (Figure 6d), they are T_bs of 1231 and 1419 cm^{-1} channels. The blue dots show the pixels identified as DCCs when BNR ≥ 1. The green dots are the pixels whose BTDs are within the noise level when BNR < 1. The red lines in Figures 6c and 6d are the simulated results of RTTOV that CTHs are set from 100 hPa to 1000 hPa. The black lines are BTD = 0. (e) The image from the MODIS visible channel.

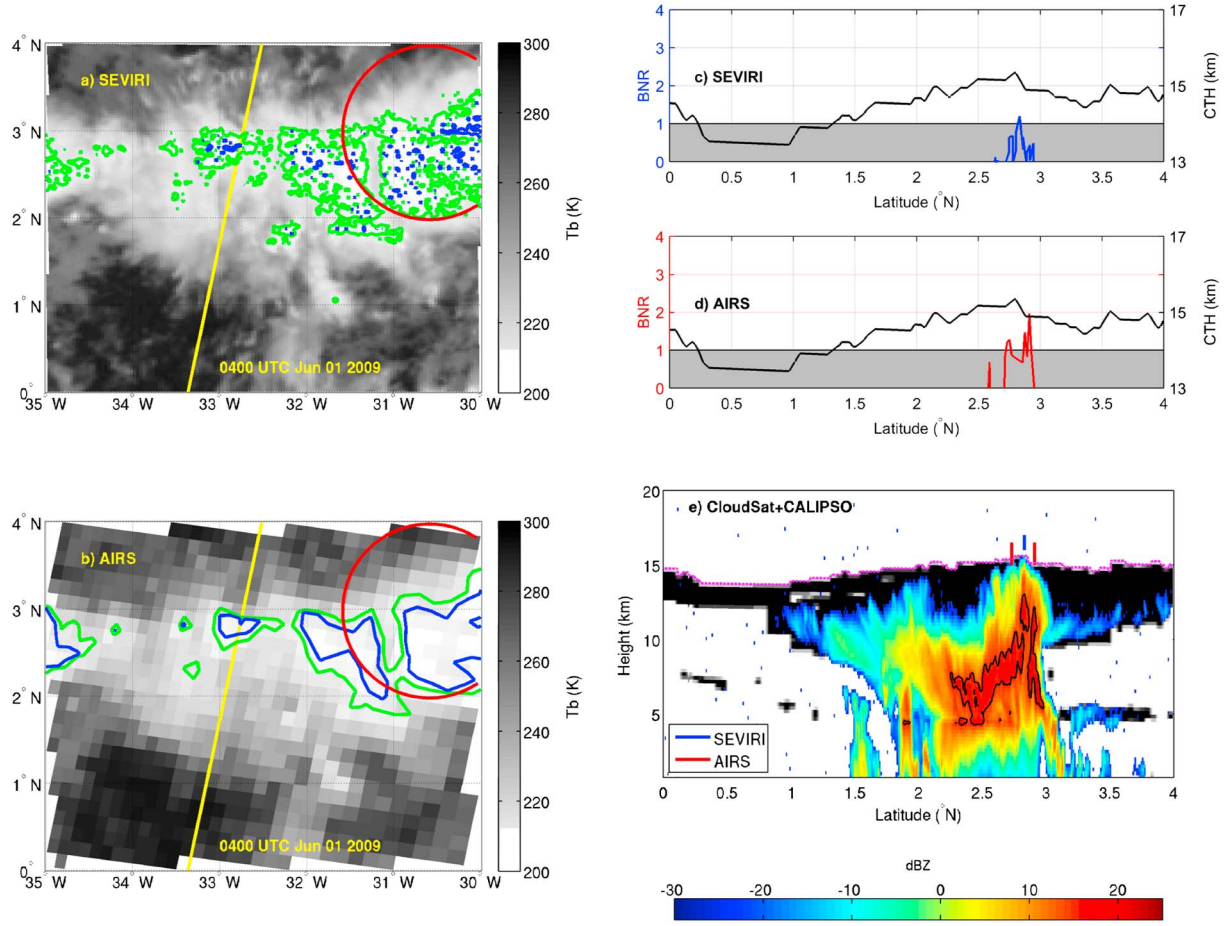

Figure 7. Brightness temperature images at 0400 UTC 1 June 2009 from the atmospheric IR window band/channel on (a) SEVIRI and (b) AIRS. The blue contours denote pixels where BNR = 1, and the green contours show pixels where BTD = 0. The red circles show the location where AF447 lost contact. The yellow lines are the trajectory of CloudSat and CALIPSO. (c and d) The BNR along the trajectory of SEVIRI and AIRS, respectively. The grey background denotes the ranges of CTH where BNR $\leq$ 1. The black line in these two panels is CTH measured by CALIPSO. (e) CloudSat and CALIPSO detections are shown. The black shadings are clouds measured by CALIPSO. Colored shadings are reflectivity measured by CloudSat. The pink dashed line marks the cloud tops as indicated by CALIPSO. The black contours inside the convective cloud show the range of radar reflectivity over 15 dB*Z*. The solid lines show the borders of DCCs identified by SEVIRI (blue) and AIRS (red) where BNR $\geq$ 1.

little or no radiation absorption. The WV band/channel on MTSAT-2, AHI, and AIRS, however, each absorbs water vapor differently. For a broadband imager such as MTSAT-2, only one WV band shows the radiation from the middle atmosphere. AHI and AIRS, however, have more WV bands/channels displaying multiple levels of WV radiation. The T_{bWV} shows a significant decline from above 400 hPa for MTSAT-2, 300 hPa for AHI, and about 200 hPa for AIRS. As the cloud top grows, the difference between T_{bIR} and T_{bWV} becomes larger for AIRS compared to MTSAT-2 and AHI. It is this sensitivity of BTD to CTH that results in the sensitivity of BNR to CTH as illustrated in Figure 4d. However, sensitivity of BTD to CTH does not occur for the MTSAT-2 imager. Sensitivity of BTD to CTH is more likely to surpass its corresponding noise and could be used to estimate CTH with an RTM. This result indicates the possibility to accurately estimate the CTH of DCCs identified by hyperspectral instruments, such as AIRS, if the atmospheric profiles are available. As noted in section 3.2 that improvement in the spectral resolution leads to better DCC identification, even as CTH becomes higher for the MTSAT-2 imager and AHI in Figure 5, the BNR value is less than 1.

Satellite images from the IR band/channel at 0600 UTC 28 December 2014 are displayed in Figures 6a, 6b, and 6e. They show the fine spatial resolution of the MTSAT-2 imager which captures the detail of the cloud edges. The T_b of the IR and WV band/channel for each pixel is plotted in the scatterplots in Figures 6c and 6d for MTSAT-2 and AIRS, respectively. DCCs are identified as BNR $\geq$ 1, and noise is defined as BNR $<$ 1. The red lines in these two panels simulated T_bs by RTTOV which represent the trend well when T_b is cold (around 200 K). The mean values of T_b for the noise pixels are both around 208 K, which is very close to the simulated

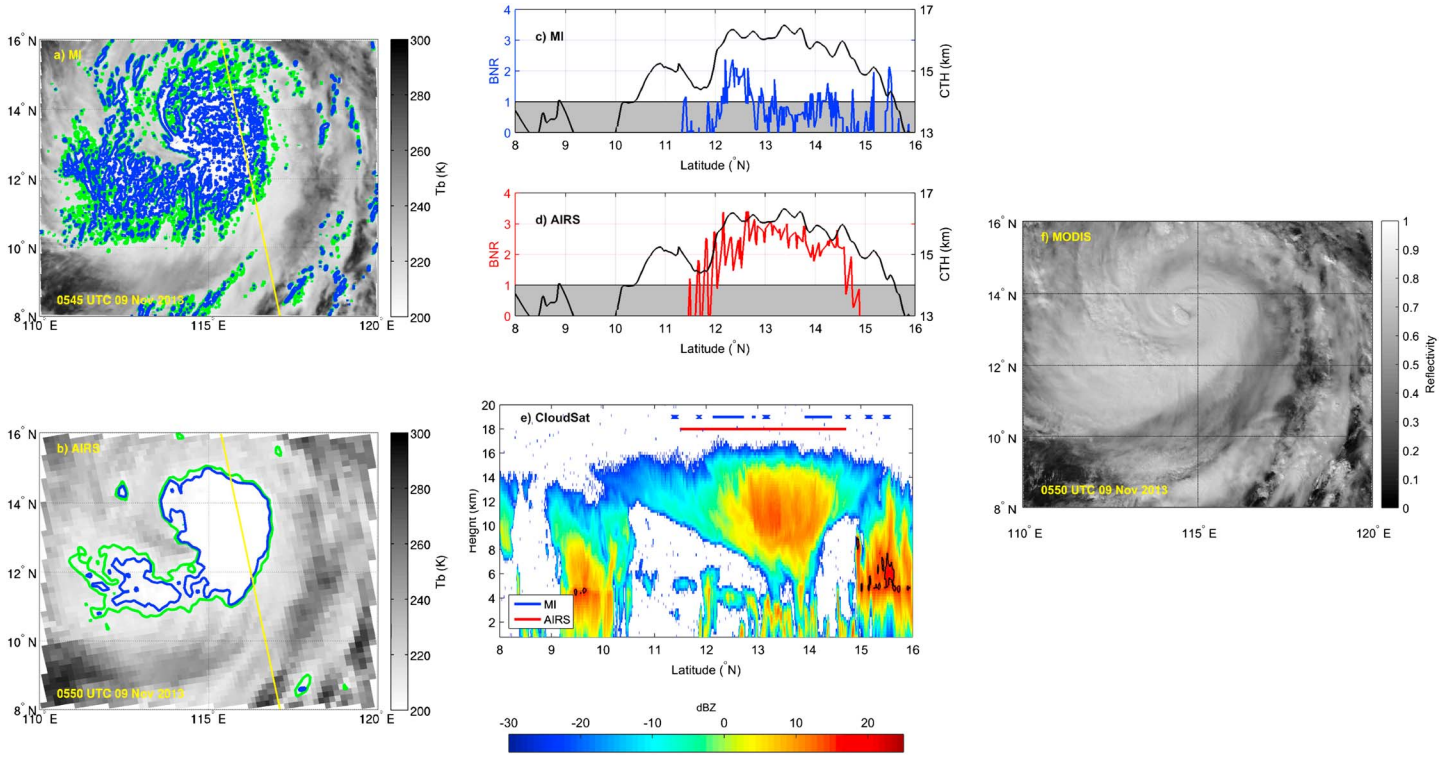

Figure 8. Brightness temperature images at about 0600 UTC 9 November 2013 from the atmospheric IR window band/channel on (a) MI and (b) AIRS. The blue contours denote pixels where BNR = 1, and the green contours show pixels where BTD = 0. The yellow lines are the trajectory of CloudSat. (c and d) The BNR along the trajectory of MI and AIRS, respectively. The grey background denotes the ranges of CTH where BNR ≤ 1. The black lines in Figures 8c and 8d are the CTH defined by −30 dB*Z* measured by CloudSat CPR. (e) CloudSat detection. Colored shadings are reflectivity measured by CloudSat. The black contours inside the convective cloud show the range of radar reflectivity over 15 dB*Z*. The solid lines show the borders of DCCs identified by MI (blue) and AIRS (red) where BNR ≥ 1. (f) The visible image from Aqua MODIS.

T_b at CCTP (Figures 5a and 5b). This result demonstrates that the simple cloud scheme assumption works well for the DCCs. The noise pixels have larger range in T_b in the MTSAT-2 image (from 188.1 to 218.6 K) than in the AIRS image (from 199.3 to 209.7 K), which also indicates that hyperspectral IR sounders perform better at DCC identification except for their coarser spatial resolution. The performance with future applications of high spatial, temporal, and spectral resolution IR sounders on board geostationary satellites [*Schmit et al.*, 2009] is anticipated to be similar.

5. Comparison With Active Remote Sensing

In this section, active remote sensing data from CloudSat/CALIPSO are applied to analyze the BTD method's ability to identify high CTH weather systems.

The AF447 case is analyzed using imagery at 0400 UTC 1 June 2009 when CloudSat/CALIPSO products are available. In Figures 7a and 7b, satellite images of the IR band/channel are displayed along with the trajectory of CloudSat/CALIPSO. Figures 7c and 7d plot the BNR of the pixels along the trajectory with the cloud range that are identified as DCCs and noise. The black lines in these two panels are the CTH derived from CALIPSO measurements. In addition, the vertical radar reflectivity (dB*Z*) and cloud fraction measured by CloudSat/CALIPSO are illustrated in Figure 7e. Despite the coarse spatial resolution of AIRS, there are fewer noise pixels along the trajectory, and the DCC part identified by AIRS includes the convective core with overshooting cloud tops where radar reflectivity is larger than 15 dB*Z* [*Alcala and Dessler*, 2002]. Only a small number of the pixels are identified as DCCs in the SEVIRI imagery. The noise range from SERIVI also covers a slightly larger area than the DCCs identified by AIRS. Furthermore, SEVIRI shows only one pixel as DCC along the CloudSat/CALIPSO trajectory (as noted by the blue line in Figure 7e), but AIRS identifies the DCC overshooting area (as marked by the red lines in Figure 7e). The overshooting area also corresponds to strong radar reflectivity from the CloudSat 2B-GEOPROF profile. Comparing Figures 7c and 7d, it seems that the BNR

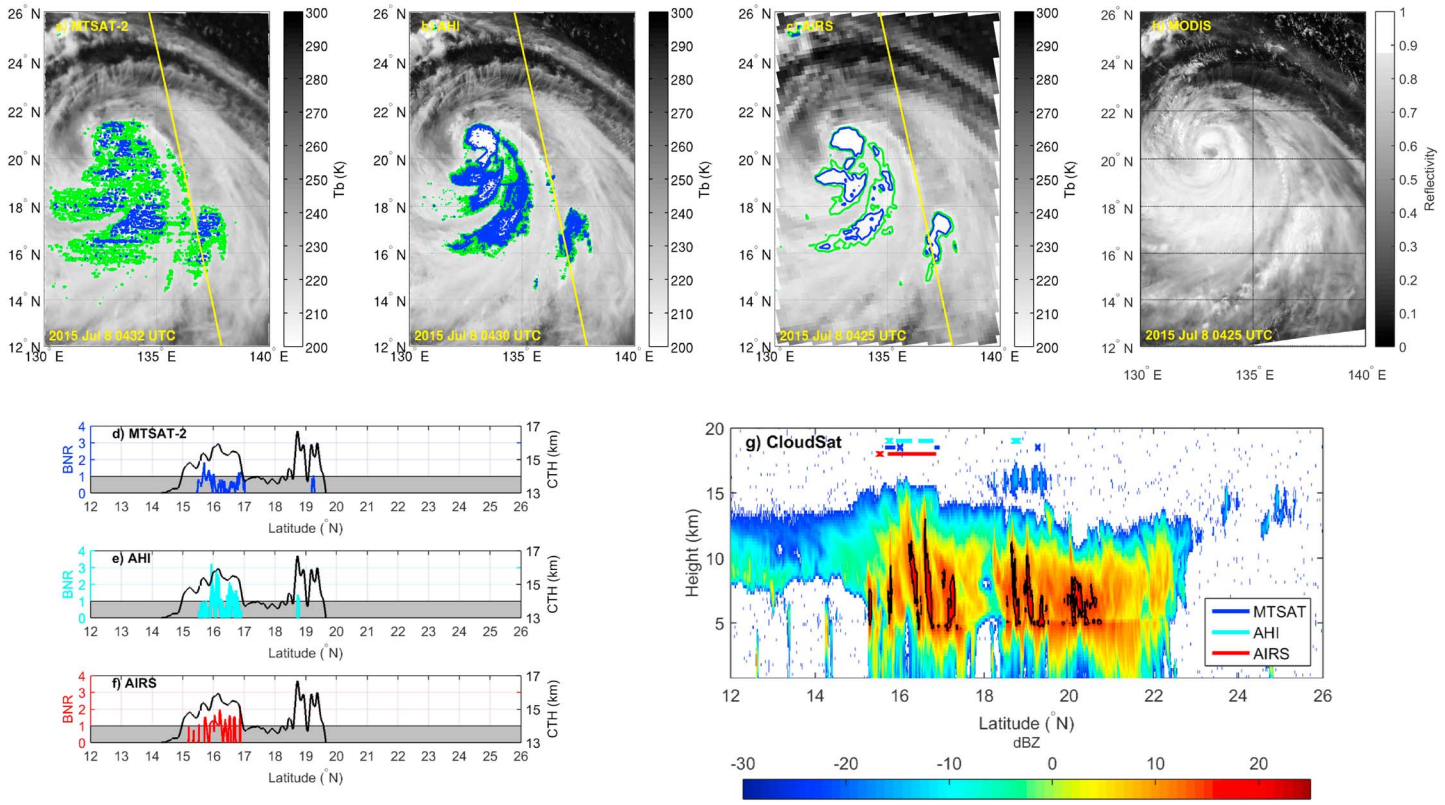

Figure 9. Brightness temperature images at around 0430 UTC 8 July 2015 from the atmospheric IR window band/channel on (a) MTSAT-2, (b) AHI, and (c) AIRS. The blue contours denote pixels where BNR = 1, and the green contours show pixels where BTD = 0. The yellow lines are the trajectory of CloudSat. (d–f) The BNR along the trajectory of MTSAT-2, AHI, and AIRS, respectively. The grey background denotes the ranges of CTH where BNR ≤ 1. The black lines in Figures 9f are the CTH defined by −30 dB*Z* measured by CloudSat CPR. (g) CloudSat detection. Colored shadings are reflectivity measured by CloudSat. The black contours inside the convective cloud show the range of radar reflectivity over 15 dB*Z*. The solid lines show the borders of DCCs identified by MTSAT-2 (blue), AHI (cyan), and AIRS (red) where BNR ≥ 1. (h) The image from the visible channel of MODIS.

detected by SEVIRI is not sensitive to high CTH, which is similar to the simulation result of the QZ8501 case for broadband instruments (Figure 4d).

As another example, we examined Supertyphoon Haiyan at approximately 0600 UTC 9 November 2013 when only the CloudSat product is available. Although the convection near the eyewall of a typhoon might not be as intense as that inside a DCC, the high cloud tops and large water vapor content are similar, which means that the BTD method also works in typhoon monitoring. Figures 8a and 8b show satellite IR images. Figure 8c and 8d plot the BNR of the pixels along the CloudSat trajectory. The CTH from CloudSat is detected as −30 dB*Z* and plotted in Figures 8c and 8d as black lines. Figure 8e displays the vertical structure of Typhoon Haiyan measured by CloudSat. Figure 8f is the visible image from Aqua MODIS. The MI noise is very close to that of MTSAT-2. It can be seen in Figures 8c and 8d that more pixels have BNR larger than 1.0 for AIRS, and the AIRS BNR also corresponds with the high cloud top better than MI. In Figure 8e, AIRS identifies an area of cloud with a CTH higher than 15 km with relative strong precipitation. For the broadband MI, the BNR along the trajectory is not as sensitive to the area of clouds with strong precipitation and higher CTH as AIRS.

The last case studied is Typhoon Linfa at about 0430 UTC 8 July 2015, for which both MTSAT-2 imager and AHI observations are available. Figures 9a–9c show satellite IR images from MTSAT-2, AHI, and AIRS. Figures 9d–9f plot the BNR of the pixels along the CloudSat trajectory as well. The black line in each panel is the highest CTH defined by −30 dB*Z*. Figure 9g displays the vertical structure of Typhoon Linfa measured by CloudSat. Figure 9h is the visible image from Aqua MODIS. Three instruments identify a similar location for the high overshooting top shown in Figures 9d–9f, and the BNR from AHI and AIRS has better correspondence with CTH. The improvement in the spatial and spectral resolution of AHI results in better performance in this case. The BNR from AHI becomes more sensitive to CTH compared to that of MTSAT-2, so that multiple bands with less noise are able to improve the DCC identification. In Figure 9a, some strange artifacts appear along the

scanline direction in the blue contours. It seems that MTSAT-2 imager due to its lower spectral resolution is not able to resolve the small difference between the values measured from the adjacent pixels along the scanline. This could be another argument for improving the spectral resolution of the instrument. In addition, AHI even outperforms AIRS in this case in terms of BNR, which can be attributed to its much finer spatial resolution being able to reveal the details of the cloud top structure. However, both MTSAT-2 and AHI detect the multiple cloud layers as DCC around 19°N, which is not identified by AIRS.

From analyzing the three cases, it can be seen that BNR measured by AIRS is very sensitive to high CTH areas where strong convection or strong precipitation occurs. The areas identified as DCCs by AIRS are more likely to meet the required detection criterion of BNR $\geq$ 1; thus, the identification is more accurate compared to broadband imagers. However, the spatial resolution of current hyperspectral IR sounders in polar orbit satellites is coarser than that of high spatial resolution broadband imagers; therefore, they cannot provide spatial details on monitoring the DCCs and other kinds of high-impact weather like typhoons and hurricanes. The next generation of advanced geostationary satellite-based imagers such as the ABI on board the U.S. GOES-R series and the AHI on board the Japanese Himawari-8 [*Kurino*, 2012; *Bessho et al.*, 2016] has even higher spatial resolution (2 km for IR bands) than the current five-band imagers and will provide detailed imagery both spatially and temporally for DCCs. There is also an improvement in the spectral resolution of WV bands for the next generation imagers. However, as indicated in this study, an advanced IR sounder in geostationary orbit could provide more accurate DCC detection.

6. Summary

In this study, a new index known as BNR is defined to evaluate the accuracy of DCC detection for different instruments using the difference between the WV and IR window radiances. If a pixel's BNR is larger than 1, the signal is stronger than noise, meaning that the pixel is part of the overshooting of the DCC. The simulation results show that instruments with higher spectral resolution have a BNR significantly larger than 1 and its value is more sensitive to CTH than instruments with a broader bandwidth, which suggests better performance in DCC identification.

The atmospheric environment of the QZ8501 case is used as input for RTTOV to simulate the $T_{b\mathrm{IR}}$ and $T_{b\mathrm{WV}}$ for both broadband imager and hyperspectral IR sounder. With a simple cloud scheme, the BTD and BNR of DCCs in tropical regions can be well simulated by RTTOV and are very close to the results from satellite measurements. Although broadband imagers on board GEO satellites (e.g., MTSAT-2 imager, SEVIRI, and MI) have finer spatial resolution and smaller noise (described by NEΔT), their BNR is closer to 1.0 and smaller when detecting DCC compared with that from hyperspectral IR sounders (e.g., AIRS and IASI). The WV channel on hyperspectral instruments detects moisture changes within a thinner layer than that on broadband instruments, which results in a more sensitive BTD value that enables more accurate DCC identification. The test of adding an additional VIIRS water vapor band shows that the smaller noise also improves the DCC identification. Besides, with improvements in spectral resolution, the next generation imagers such as AHI on board the Japanese Himawari-8/Himawari-9, the ABI on board the U.S. Geostationary Operation Environmental Satellite (GOES)-R series, the Advanced Geosynchronous Radiation Imager (AGRI) on board the Chinse FengYun (FY)-4 series [*Yang et al.*, 2016] not only provide imagery with higher definition but will also detect DCCs with a larger BNR, because those new WV bands are able to detect moisture at different atmospheric levels [*Di et al.*, 2016]. Additionally, a hyperspectral instrument [*Schmit et al.*, 2009] on board the geostationary satellite, such as the Geosynchronous Interferometric Infrared Sounder (GIIRS) on board FY4A launched on 11 December 2016, has the potential to estimate CTH for DCC evolution because its BNR is significantly larger than 1.0 and very sensitive to CTH. Those advanced imagers and sounder on board the new generation of geostationary weather and environmental satellites provide DCC information with better accuracy and high temporal and spatial resolutions.

With active remote sensing data from CloudSat/CALIPSO, the analysis of the AF447, Typhoon Haiyan, and Typhoon Linfa cases also validates the sensitivity of BNR in high CTH identification by the BTD method using AIRS and AHI. The BNR from AIRS and AHI is more consistent with high CTH than that from current generation imagers. Nevertheless, the imagers, especially the next generation of imagers on board GEO satellites, still have advantages in temporal and spatial resolution, giving detailed images showing DCCs. Based on the test and analysis in this paper, when trying to improve VIIRS by adding an additional water vapor band(s), it is recommended that both better SNR and spectral resolution should be considered for accurate DCC detection,

which is very useful for shortwave band calibration and validation. Since the advanced imagers have visible, near-infrared, and infrared bands with high spatial resolution, and the advanced IR sounder has high spectral resolution, both an advanced imager and an advanced IR sounder are desired on board the same geostationary platform for better cloud characterization [*Li et al.*, 2004a; 2004b, 2005a, 2005b] continuous DCC detection and monitoring. Testing high cloud detection with advanced instrument in future work will also include more cases of high-impact weather such as supercells, large hail, tornadoes, and hurricanes.

Acknowledgments
The RTTOV model in this study was run on computers provided by the University of Wisconsin-Madison Space Science Engineering Center (SSEC). ECMWF is thanked for the operational model analysis data set. The data from AIRS, MTSAT-2, COMS-1, and Himawari-8 imagery were obtained from SSEC's Data Center at the University of Wisconsin-Madison (http://www.ssec.wisc.edu/datacenter/). The CloudSat/CAPLISO data were obtained freely from the CloudSat Data Processing Center (http://www.cloudsat.cira.colostate.edu). This work was completed during Y. Ai and W. Shi's visit to the University of Wisconsin-Madison funded by the China Scholarship Council (CSC). This research is partly supported by the NOAA GOES-R high-impact weather and proving ground programs and the JPSS algorithm project. Tim Schmit, NOAA NESDIS STAR, is thanked for constructive comments on this manuscript. The views and opinions expressed in this article are those of the authors and do not necessarily reflect the official policy of any agency of the U.S. government.

References

Ackerman, S. A. (1996), Global satellite observations of negative brightness temperature differences between 11 and 6.7 μm, *J. Atmos. Sci.*, *53*(19), 2803–2812.

Ai, Y., W. Li, Z. Meng, and J. Li (2016), Life cycle characteristics of MCSs in middle east China tracked by geostationary satellite and precipitation estimates, *Mon. Weather Rev.*, *144*(2016), 2517–2530.

Alcala, C., and A. Dessler (2002), Observations of deep convection in the tropics using the Tropical Rainfall Measuring Mission (TRMM) precipitation radar, *J. Geophys. Res.*, *107*(D24).

Aminou, D. (2002), MSG's SEVIRI instrument, *ESA Bull.*, *0376-4265*(111), 15–17.

Aumann, H., and A. Ruzmaikin (2013), Frequency of deep convective clouds in the tropical zone from 10 years of AIRS data, *Atmos. Chem. Phys.*, *13*(21), 10,795–10,806.

Aumann, H., S. Broberg, D. Elliott, S. Gaiser, and D. Gregorich (2006), Three years of Atmospheric Infrared Sounder radiometric calibration validation using sea surface temperatures, *J. Geophys. Res.*, *111*, D16S90.

Aumann, H., S. DeSouza-Machado, and A. Behrangi (2011), Deep convective clouds at the tropopause, *Atmos. Chem. Phys.*, *11*(3), 1167–1176.

Aumann, H. H., and R. J. Pagano (1994), Atmospheric infrared sounder on the Earth Observing System, *Opt. Eng.*, *33*(3), 776–784.

Aumann, H. H., et al. (2003), AIRS/AMSU/HSB on the Aqua mission: Design, science objectives, data products, and processing systems, *IEEE Trans. Geosci. Remote Sens.*, *41*(2), 253–264.

Bedka, K., J. Brunner, R. Dworak, W. Feltz, J. Otkin, and T. Greenwald (2010), Objective satellite-based detection of overshooting tops using infrared window channel brightness temperature gradients, *J. Appl. Meteorol. Climatol.*, *49*(2), 181–202.

Bedka, K. M. (2011), Overshooting cloud top detections using MSG SEVIRI infrared brightness temperatures and their relationship to severe weather over Europe, *Atmos. Res.*, *99*(2), 175–189.

Bedka, K. M., R. Dworak, J. Brunner, and W. Feltz (2012), Validation of satellite-based objective overshooting cloud-top detection methods using CloudSat Cloud Profiling Radar observations, *J. Appl. Meteorol. Climatol.*, *51*(10), 1811–1822.

Bessho, K., et al. (2016), An introduction to Himawari-8/9—Japan's new-generation geostationary meteorological satellites, *J. Meteorol. Soc. Jpn*, *94*(2), 151–183.

Bloom, H. J. (2001), The cross-track infrared sounder (CrIS): A sensor for operational meteorological remote sensing, in *Geoscience and Remote Sensing Symposium, 2001. IGARSS'01. IEEE 2001 International*, vol. 3, pp. 1341–1343, IEEE, Sydney, Australia.

Chalon, G., F. Cayla, and D. Diebel (2001), IASI—An advanced sounder for operational meteorology, in *Proceedings of the 52nd IAF, International Astronautical Congress*, pp. 1–5, Centre National d'Etudes Spatiales, Toulouse, France.

Chemel, C., M. R. Russo, J. A. Pyle, R. S. Sokhi, and C. Schiller (2009), Quantifying the imprint of a severe Hector thunderstorm during ACTIVE/SCOUT-O3 onto the water content in the upper troposphere/lower stratosphere, *Mon. Weather Rev.*, *137*(8), 2493–2514.

Cho, Y.-M., and H.-S. Youn (2006), Characteristics of COMS meteorological imager, in *Remote Sensing*, pp. 63,611G–63,611G, International Society for Optics and Photonics, Stockholm.

Conway, E. D. (1997), *An Introduction to Satellite Image Interpretation*, The Johns Hopkins Univ. Press, Baltimore, Md.

Di, D., Y. Ai, J. Li, W. Shi, and N. Lu (2016), Geostationary satellite-based 6.7 μm band best water vapor information layer analysis over the Tibetan Plateau, *J. Geophys. Res. Atmos.*, *121*(9), 4600–4613.

Eyre, J. (1991), *A Fast Radiative Transfer Model for Satellite Sounding Systems*, European Centre for Medium-Range Weather Forecasts, Reading, U. K.

Eyre, J. R., and W. P. Menzel (1989), Retrieval of cloud parameters from satellite sounder data: A simulation study, *J. Appl. Meteorol.*, *28*(4), 267–275.

Kurino, T. (1997), A satellite infrared technique for estimating "deep/shallow" precipitation, *Adv. Space Res.*, *19*(3), 511–514.

Kurino, T. (2012), *Future plan and recent activities for the Japanese follow-on geostationary meteorological satellite Himawari-8/9*, Abstract IN43E-03 presented at 2012 Fall Meeting, vol. 1, AGU.

Lane, T. P., R. D. Sharman, T. L. Clark, and H.-M. Hsu (2003), An investigation of turbulence generation mechanisms above deep convection, *J. Atmos. Sci.*, *60*(10), 1297–1321.

Li, J., W. P. Menzel, and A. J. Schreiner (2001), Variational retrieval of cloud parameters from GOES sounder longwave cloudy radiance measurements, *J. Appl. Meteorol.*, *40*(3), 312–330.

Li, J., W. P. Menzel, F. Sun, T. J. Schmit, and J. Gurka (2004a), AIRS subpixel cloud characterization using MODIS cloud products, *J. Appl. Meteorol.*, *43*(8), 1083–1094.

Li, J., W. P. Menzel, W. Zhang, F. Sun, T. J. Schmit, J. J. Gurka, and E. Weisz (2004b), Synergistic use of MODIS and AIRS in a variational retrieval of cloud parameters, *J. Appl. Meteorol.*, *43*(11), 1619–1634.

Li, J., H.-L. Huang, C.-Y. Liu, P. Yang, T. J. Schmit, H. Wei, E. Weisz, L. Guan, and W. P. Menzel (2005a), Retrieval of cloud microphysical properties from MODIS and AIRS, *J. Appl. Meteorol.*, *44*(10), 1526–1543.

Li, J., C.-Y. Liu, H.-L. Huang, T. J. Schmit, X. Wu, W. P. Menzel, and J. J. Gurka (2005b), Optimal cloud-clearing for AIRS radiances using MODIS, *IEEE Trans. Geosci. Remote Sens.*, *43*(6), 1266–1278.

Mace, G. G., and Q. Zhang (2014), The Cloudsat Radar-Lidar Geometrical Profile product (RL-GEOPROF): Updates, improvements, and selected results, *J. Geophys. Res. Atmos.*, *119*(15), 9441–9462.

Machado, L., W. Rossow, R. Guedes, and A. Walker (1998), Life cycle variations of mesoscale convective systems over the Americas, *Mon. Weather Rev.*, *126*(6), 1630–1654.

Machado, L. A., W. F. Lima, O. Pinto, and C. A. Morales (2009), Relationship between cloud-to-ground discharge and penetrative clouds: A multi-channel satellite application, *Atmos. Res.*, *93*(1), 304–309.

Mapes, B. E., and R. A. Houze (1993), Cloud clusters and superclusters over the oceanic warm pool, *Mon. Weather Rev.*, *121*(5), 1398–1416.

Marchand, R., G. G. Mace, T. Ackerman, and G. Stephens (2008), Hydrometeor detection using Cloudsat—An Earth-orbiting 94 GHz cloud radar, *J. Atmos. Oceanic Technol.*, *25*(4), 519–533.
Martin, D. W., R. A. Kohrs, F. R. Mosher, C. M. Medaglia, and C. Adamo (2008), Over-ocean validation of the global convective diagnostic, *J. Appl. Meteorol. Climatol.*, *47*(2), 525–543.
Mathon, V., and H. Laurent (2001), Life cycle of Sahelian mesoscale convective cloud systems, *Q. J. R. Meteorol. Soc.*, *127*(572), 377–406.
Matricardi, M., F. Chevallier, and S. Tjemkes, (2001), An improved general fast radiative transfer model for the assimilation of radiance observations, ECMWF research Dept. Tech. Rep., Tech. Memo., 345 pp., ECMWF. [Available online at http://www.ecmwf.int/publications.]
Puschell, J. J., et al. (2006), In-flight performance of the Japanese Advanced Meteorological Imager, in *SPIE Optics+ Photonics*, pp. 62,960N–62,960N, International Society for Optics and Photonics, San Diego, Calif.
Qie, X., X. Wu, T. Yuan, J. Bian, and D. Lu (2014), Comprehensive pattern of deep convective systems over the Tibetan Plateau–South Asian Monsoon region based on TRMM data, *J. Clim.*, *27*(17), 6612–6626.
Reynolds, D. W. (1980), Observations of damaging hailstorms from geosynchronous satellite digital data, *Mon. Weather Rev.*, *108*(3), 337–348.
Saunders, R., M. Matricardi, and P. Brunel (1999), An improved fast radiative transfer model for assimilation of satellite radiance observations, *Q. J. R. Meteorol. Soc.*, *125*(556), 1407–1425.
Schmetz, J., S. Tjemkes, and M. Gube (1997), Monitoring deep convection and convective overshooting with MeteoSat, *Adv. Space Res.*, *19*(3), 433–441.
Schmetz, J., P. Pili, S. Tjemkes, D. Just, J. Kerkmann, S. Rota, and A. Ratier (2002), An introduction to MeteoSat Second Generation (MSG), *Bull. Am. Meteorol. Soc.*, *83*(7), 977–992.
Schmetz, J., M. König, P. Pili, S. Rota, A. Ratier, and S. Tjemkes (2003), 7.3 Meteosat Second Generation (MSG): Status after launch, in *Proceedings of the 12th Conference on Satellite Meteorology and Oceanography*, Long Beach, Calif.
Schmit, T. J., et al. (2005), Introducing the next-generation advanced baseline imager on GOES-R, *Bull. Am. Meteorol. Soc.*, *86*(8), 1079–1096.
Schmit, T. J., J. Li, S. A. Ackerman, and J. J. Gurka (2009), High-spectral-and high-temporal-resolution infrared measurements from geostationary orbit, *J. Atmos. Oceanic Tech.*, *26*(11), 2273–2292.
Schmit, T. J., P. Griffith, M. M. Gunshor, J. M. Daniels, S. J. Goodman, and W. J. Lebair (2017), A Closer Look at the ABI on the GOES-R Series, *Bull. Am. Meteorol. Soc.*, doi:10.1175/BAMS-D-15-00230.1, in press.
Setvák, M., D. T. Lindsey, R. M. Rabin, P. K. Wang, and A. Demeterová (2008), Indication of water vapor transport into the lower stratosphere above midlatitude convective storms: MeteoSat Second Generation satellite observations and radiative transfer model simulations, *Atmos. Res.*, *89*(1), 170–180.
Setvák, M., K. Bedka, D. T. Lindsey, A. Sokol, Z. Charvát, J. Šťástka, and P. K. Wang (2013), A-Train observations of deep convective storm tops, *Atmos. Res.*, *123*, 229–248.
Shimamura, A. (1999), MSAS (MTSAT satellite-based augmentation system) project status, *Air & Space Europe*, *1*(2), 63–67.
Stephens, G. L., et al. (2002), The Cloudsat mission and the A-Train: A new dimension of space-based observations of clouds and precipitation, *Bull. Am. Meteorol. Soc.*, *83*(12), 1771–1790.
Tang, X., and B. Chen (2006), Cloud types associated with the Asian summer monsoons as determined from MODIS/TERRA measurements and a comparison with surface observations, *Geophys. Res. Lett.*, *33*, L07814, doi:10.1029/2006GL026004.
Wei, H., P. Yang, J. Li, B. A. Baum, H.-L. Huang, S. Platnick, Y. Hu, and L. Strow (2004), Retrieval of semitransparent ice cloud optical thickness from Atmospheric Infrared Sounder (AIRS) measurements, *IEEE Trans. Geosci. Remote Sens.*, *42*(10), 2254–2267.
Welsch, C., H. Swenson, S. A. Cota, F. DeLuccia, J. M. Haas, C. Schueler, R. M. Durham, J. E. Clement, and P. E. Ardanuy (2001), VIIRS (Visible Infrared Imager Radiometer Suite): A next-generation operational environmental sensor for NPOESS, in *Geoscience and Remote Sensing Symposium, 2001. IGARSS'01. IEEE 2001 International*, vol. 3, pp. 1020–1022, IEEE, Sydney, Australia.
Wu, X., X. Qie, and T. Yuan (2013), Regional distribution and diurnal variation of deep convective systems over the Asian monsoon region, *Sci. China Earth Sci.*, *56*(5), 843–854.
Yang, J., Z. Zhang, C. Wei, F. Lu, and Q. Guo (2016), Introducing the new generation of Chinese geostationary weather satellites–FenYun 4 (FY-4), *Bull. Am. Meteorol. Soc.*, doi:10.1175/BAMS-D-16-0065.1, in press.
Young, A. H., J. J. Bates, and J. A. Curry (2012), Complementary use of passive and active remote sensing for detection of penetrating convection from Cloudsat, CALIPSO, and Aqua MODIS, *J. Geophys. Res.*, *117*(D13), D13205, doi:10.1029/2011JD016749.